Electrokinetics in two-dimensional complicated geometries: Conformal mapping and experimental comparison

Zhibo Gu,[1] Peng Huo,[1] Bingrui Xu, Mingzhuo Su,[1] Martin Z. Bazant,[2,*] and Daosheng Deng[1,†]
[1]*Department of Aeronautics and Astronautics, Fudan University, Shanghai 200433, China*
[2]*Department of Chemical Engineering and Department of Mathematics, Massachusetts Institute of Technology, Cambridge, Massachusetts 02139, USA*

(Received 7 September 2021; accepted 22 February 2022; published 11 March 2022)

In this paper, we explore the electrokinetics in the complex two-dimensional geometries via conformal mapping and experimental comparison. A general theoretical frame of conformal mapping is provided for the application in electrokinetics, and three geometries are taken as an example to derive concentration polarization, potential, and electric field. For an eccentric annulus, the theoretical calculation of limiting current remarkably agrees with the experimental measurement, indicating that conformal mapping as a powerful approach is applicable for the ion transport. In the overlimiting current, the asymmetric electroconvection and deionization shock in experiments are qualitatively consistent with the asymmetric slip velocity associated with the electric field from conformal mapping. Then for the concentric ellipse geometry, when the inner ellipse squashes into a finite stripe, the local electric field at the tips tends to form a singularity, driving the electro-osmotic instability of concentration enrichment. Additionally, for a corner geometry, the intensity of the electric field is analyzed for different shapes. Hence, conformal mapping as a theoretical tool potentially inspires more future work for the electrokinetics in the complicated geometries, while the experimental findings, particularly the stronger concentration depletion induced by eccentricity, hold the promising applications, such as the shock electrodialysis for the deionization and water treatment, and electrophoresis for the particle manipulation in microfluidic devices.

DOI: 10.1103/PhysRevFluids.7.033701

I. INTRODUCTION

Electrokinetics in microstructures and complex geometries plays a significant role for electrochemical systems and microfluidic devices [1–3] for desalination [4], radionuclides treatment [5], and biomolecules separation [6,7]. In the bulk, the electro-osmotic instability (EOI) or the electroconvection instability originates from the extended space charges in the overlimiting current (OLC) [8,9]. At the reduced length scale in microchannels or the porous media, deionization shocks arise from the surface charges, leading to the development of the shock electrolysis [4,10–12]. Recently, in a concentric annulus geometry (the inner electrode is placed in the center, while the outer electrode is the circular ring), the electroconvection-driven deionization is identified [13], and the electro-osmotic instability of concentration enrichment in an aqueous electrolyte is established, because of the strong electric field arising from the line charge singularity [14].

Besides designing structure geometry and tailing the length scale, the asymmetry or symmetry breaking provides another degree of freedom to manipulate the ion transport, significantly enriching

*bazant@mit.com
†dsdeng@fudan.edu.cn

the electrokinetics phenomena. For example, various asymmetries-controlled potential, irregular shape and nonuniform surface properties can produce the induced-charge electro-osmotic flow [15]. The spatial asymmetry generates a net pumping of fluid past the polarizable bodies (e.g., metals) by the electro-osmotic flow or the translation and rotation for a freely suspended colloidal particle by induced-charged electrophoresis [16].

Consequently, the complicated geometries together with asymmetries might offer opportunities to further unravel more electrokinetic phenomenon. For example, in an annulus geometry [13,14], the asymmetric electrodes (the inner electrode is aligned in an off-center fashion, while the outer electrode is still the circular ring) might cause the asymmetry of the electric field, consequently affecting the concentration polarization, electroconvection, and shock deionization. However, the complex geometries and the asymmetries not only hinder the direct derivation of analytical solutions in the mathematic analysis but also increase the computational cost and numerical difficulty for the numerical simulation.

As one of the elegant mathematical approaches, conformal mapping based on the principle of "Loewner chains" has the unique capability to tackle the complicated irregular geometries. By mapping an irregular geometry into a regular domain to be solvable easily or with an available analytical solution, the physical quantities in the complicated shapes can be obtained by the opposite mapping. Indeed, conformal mapping has been applied to a broad range of the subjects, such as solving the Helmholtz equation for acoustic wave scattering [17], investigating the coriolis effects on rotating Hele-Shaw flows [18], studying the nonharmonic functions in transport theory [19], the non-Laplacian growth phenomena [20], interfacial morphology dynamics [21], and interfacial dynamics in transport-limited dissolution [22,23].

In this paper, by utilizing conformal mapping and experimental comparison, the electrokinetics in the complicated two-dimensional (2D) geometries is investigated. A general theory of conformal mapping in two-dimensional geometry is presented in Sec. II. Then the electrokinetics in an eccentric annulus is thoroughly surveyed in Sec. III, including concentration polarization, limiting current, electroconvection, and deionization shock. Moreover, the general applicability of conformal mapping for more complex geometries are demonstrated by the concenter ellipse geometry (Sec. IV) and the corner geometry (Sec. V). Last, the discussion and outlook are provided in Sec. VI.

II. GENERAL THEORY OF CONFORMAL MAPPING IN A TWO-DIMENSIONAL GEOMETRY

The Nernst-Planck equations for steady state without flow in a dilute, binary electrolyte are in a special class of conformally invariant systems of nonlinear partial differential equations, for which exact solutions can be derived in any two-dimensional geometry from the solution in a simple rectangular or concentric annular geometry by conformal mapping [19]. The solutions still hold even as the electrodes slowly change shape by electrodeposition at the cathode and electrodissolution at the anode, as long as the ion transport is quasisteady [20].

In a general case, we consider a binary electrolyte confined to a domain Ω_z in the $z = x + yi$ plane between a cathode curve C_z and anode curve A_z. The dimensionless equations of ion concentration c and electric potential φ for the quiescent state of steady ionic current (prior to hydrodynamic instability) [14,19] are

$$\nabla^2 c = 0, \tag{1a}$$

$$\nabla \cdot (c\nabla\varphi) = 0, \tag{1b}$$

with boundary conditions

$$\varphi = 0 \text{ on } C_z, \quad \varphi = V \text{ on } A_z. \tag{2}$$

Two integral constraints are imposed here. One integral constraint specifies the total current,

$$I = \int_{C_z} 2\hat{n} \cdot \nabla c dl = -\int_{A_z} 2\hat{n} \cdot \nabla c dl, \tag{3}$$

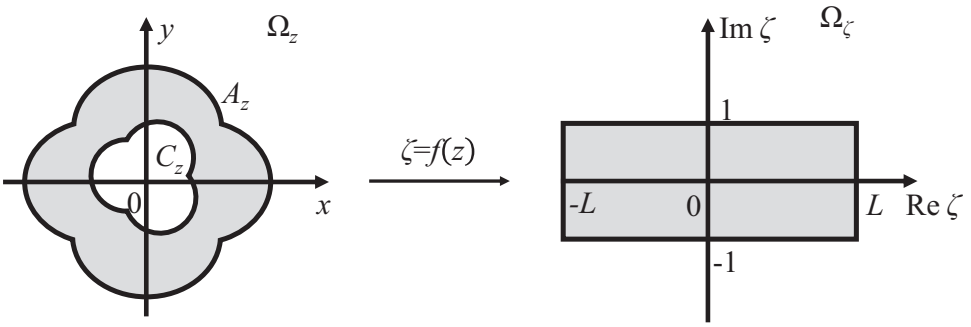

FIG. 1. A physical region Ω_z is conformally mapped to a mathematic region Ω_ζ of a rectangular domain

where $\hat{n}$ is the normal direction vector at the interface. The other constrain normalizes the total species amount,

$$\iint_{\Omega_z} c dx dy = \iint_{\Omega_z} dx dy = \mathscr{C}_z. \tag{4}$$

The last condition of Eq. (4) is not conformally invariant and changes with different mapping. Nevertheless the general solution in any 2D geometry is still obtained, since the concentration normalization $\mathscr{C}_z$ only affects a constant in the solution.

A. Conformal mapping to a rectangular domain

Let $\zeta = f(z)$ be the conformal map from a physical domain Ω_z in the z plane to a rectangular domain (Fig. 1), $|\mathrm{Im}\ \zeta| < 1$, $|\mathrm{Re}\ \zeta| < L$, in the mathematical ζ plane. The anode is the image of $\mathrm{Im}\ \zeta = 1$, and the cathode is the image of $\mathrm{Im}\ \zeta = -1$. The solutions have a general form as below [19],

$$c(x, y) = \frac{I_{\mathrm{lim}}}{2L}[1 + \tilde{I}\mathrm{Im} f(z)], \tag{5a}$$

$$\varphi(x, y) = \ln\left[\frac{1 + \tilde{I}\mathrm{Im} f(z)}{1 - \tilde{I}}\right], \tag{5b}$$

$$\tilde{I} = \frac{e^V - 1}{e^V + 1}, \tag{5c}$$

where $\tilde{I} = I/I_{\mathrm{lim}}$ is a dimensionless current scaled to the limit current in the mapping geometry. Indeed, the simple solution for parallel-plate electrodes has been conformally mapped to semi-infinite plates and misaligned coaxial cylinders [19].

Representing vectors as complex numbers, the electric field in the z plane is given by the complex gradient operator acting on the potential, $E_z = -\nabla_z \varphi$, which transforms via $\nabla_z = \overline{f'(z)}\nabla_\zeta$ to the ζ plane where the electric field is aligned with the imaginary axis [for example, in a rectangular coordinate system, $\nabla_z = \partial/\partial x + i\partial/\partial y$ and $\nabla_\zeta = \partial/\partial \mathrm{Re} f(z) + i\partial/\partial \mathrm{Im} f(z)$]. The electric field everywhere in the physical domain Ω_z is thus given by

$$|E_z| = \frac{|f'(z)|\tilde{I}}{1 + \tilde{I}\mathrm{Im} f(z)}. \tag{6}$$

The electric field at the cathode [$\mathrm{Im} f(z) = -1$] is

$$|E|_{C_z} = \frac{|f'(z)|\tilde{I}}{1 - \tilde{I}}. \tag{7}$$

And the electric field at the anode [$\mathrm{Im} f(z) = 1$] is

$$|E|_{A_z} = \frac{|f'(z)|\tilde{I}}{1+\tilde{I}}, \tag{8}$$

which tends to a universal value at the limiting current, entirely determined by the geometry (conformal map):

$$|E|_{A_z} \to \frac{|f'(z)|}{2}. \tag{9}$$

For example, the conformal mapping to a circular geometry is defined by the logarithm map ($L = \pi$, χ for the inner radius of the inner anode) [14],

$$f(z) = -i\left(1 - \frac{2\ln z}{\ln \chi}\right), \tag{10}$$

and then

$$|E|_{\text{anode}} \to \frac{-1}{\chi \ln \chi}. \tag{11}$$

The electric field has a tendency to approach an infinite singularity, resulting in the intriguing electro-osmotic instability of concentration enrichment [14].

B. Analytic solution in a concentric annulus

The electrokinetics in an concentric annulus has been investigated theoretically and experimentally, and an analytic solution is identified for concentration polarization and electric potential, and current-voltage relationship in the region of underlimiting current and limiting current [13,14]. Let us consider the following model problem in mathematical region Ω_ζ of a concentric annulus to attain its analytic solution. A dilute, binary $z:z$ electrolyte with concentration (c_0) fills a circular channel with an inner radius (κ) and outer radius 1 under an applied voltage. In the steady state, under the assumption of the azimuthal symmetry and charge neutrality, the Nernst-Planck equations are simplified into a 1D dimensionless form as below [13]:

$$\frac{dc}{dr} + c\frac{d\varphi}{dr} = -\frac{I}{2\pi r}, \tag{12a}$$

$$\frac{dc}{dr} - c\frac{d\varphi}{dr} = 0. \tag{12b}$$

Equation (12a) shows the cation flux responsible for the current density, while Eq. (12b) implies the zero anion flux for an ideal cation-selective surface. Here $c = c_+ = c_-$ is the (equal) dimensionless mean concentration of cations and anions scaled by c_0, r is dimensionless radius in Ω_ζ, φ the dimensionless potential scaled by the thermal voltage, k_BT/ze, and I is the dimensionless current scaled by $zeDc_0$, assuming equal diffusivity D for cations and anions [13].

The concentration polarization and the electric potential in the annulus Ω_ζ is obtained by the above Eq. (12),

$$c(r) = 1 - \frac{I}{4\pi}\left(\ln r + \frac{1}{2} + \frac{\kappa^2 \ln \kappa}{1-\kappa^2}\right), \tag{13a}$$

$$\varphi(r) = \ln c(r) + \text{const}. \tag{13b}$$

In the case of the inner cathode electrode or under the positive voltage bias, the limiting current is obtained from Eq. (13a) by $c(\kappa) = 0$ for the zero concentration at the cathode,

$$I = -8\pi \frac{(1-\kappa^2)}{1 + 2\ln\kappa - \kappa^2}. \tag{14a}$$

Similarly, in the case of the inner anode electrode or under the negative voltage bias, the limiting current is obtained from Eq. (13a) by $c(1) = 0$ for the zero concentration at the cathode,

$$I = 8\pi \frac{(1-\kappa^2)}{1 + 2\kappa^2 \ln \kappa - \kappa^2}. \tag{14b}$$

Using conformal mapping, the electric field E_z in physical region Ω_z is calculated in the mathematical ζ plane as follows:

$$E_z = -\nabla_z \varphi = -\overline{f'(z)} \nabla_\zeta \varphi = \overline{f'(z)} E_\zeta. \tag{15}$$

The complex geometries can be mapped to this concentric annulus by transformation, and the attained theory can be subsequently compared with experiments. The eccentric annulus, the concentric ellipse, and the corner geometry are taken as an example to be investigated.

III. AN ECCENTRIC ANNULUS GEOMETRY

We proceed to examine the concentration polarization, limiting current, electroconvection and deionization shock, and electro-osmotic instability of concentration enrichment in an eccentric annulus geometry by misaligning the central electrode.

A. Conformal mapping of an eccentric annulus to a concentric annulus

We consider an eccentric annulus with an inner radius χ, an outer radius 1, and an eccentricity e in a z plane [Fig. 2(a)],

$$\{\Omega_z \mid |z| < 1, |z - e| > \chi, 0 < e < 1 - \chi\}. \tag{16}$$

By conformal mapping $\zeta = f(z)$, the eccentric ring is mapped to a concentric annulus (an inner radius κ and an outer radius 1) in ζ plane $\{\Omega_\zeta \mid \kappa < |\zeta| < 1\}$ [Fig. 2(a)]. According to Refs. [14,19], the formation of the mapping is

$$\zeta = f(z) = \frac{z - \alpha}{\alpha z - 1}, |\alpha| < 1. \tag{17}$$

The linear fractional transformations always map a circle to a circle. Obviously, $f(z)$ maps the $|z| = 1$ to $|\zeta| = 1$, independent on α. Therefore, only a particular value of α is to be identified, which maps the inner circle $|z - e| = \chi$ to a circle of the form $|\zeta| = \kappa$.

In order to map the points $e - \chi$ and $e + \chi$ on the inner circle to the points κ and $-\kappa$ on the circle $|\zeta| = \kappa$, α is required to satisfy with the following condition:

$$f(e + \chi) = \frac{e + \chi - \alpha}{\alpha(e + \chi) - 1} = -\kappa, \tag{18a}$$

$$f(e - \chi) = \frac{e - \chi - \alpha}{\alpha(e - \chi) - 1} = \kappa. \tag{18b}$$

Then from Eqs. (18a) and (18b), α and κ are obtained,

$$\alpha = \frac{-(\chi^2 - e^2 - 1) - \sqrt{(\chi^2 - e^2 - 1)^2 - 4e^2}}{2e}, \tag{19a}$$

$$\kappa = \kappa(e, \chi) = \frac{e - \chi - \alpha}{\alpha(e - \chi) - 1}, \tag{19b}$$

where κ has an analytical solution with a complicated expression. Thus, the eccentric annuluses with a given radius χ and eccentricity e can be conformally mapped into the annuluses with an inner radius κ.

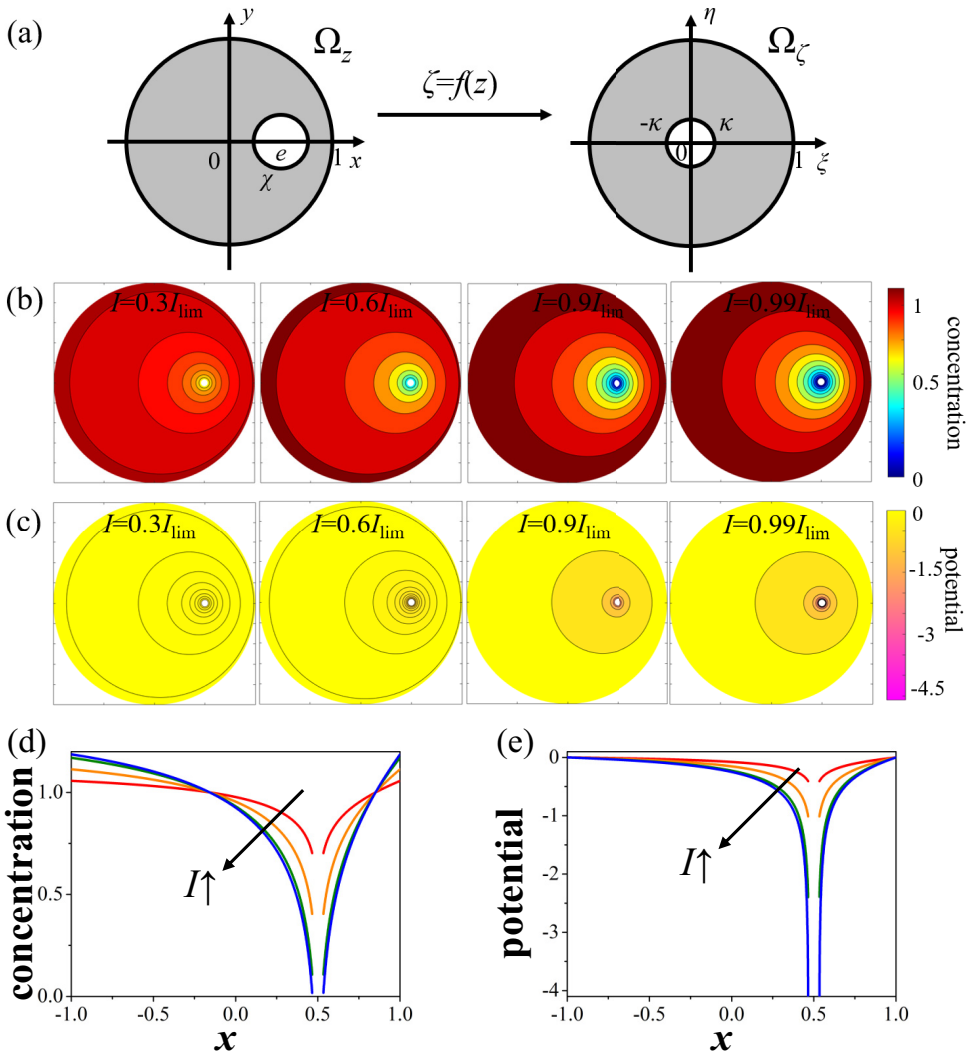

FIG. 2. Concentration polarization and potential distribution dependent on the current in an eccentric annulus ($e = 1/2$, $\chi = 1/30$). (a) A physical region Ω_z of an eccentric annulus is conformally mapped to a mathematic region Ω_ζ of a concentric annulus. (b) Concentration polarization and (c) electric potential dependent on current ($I = 0.3$, 0.6, 0.9, and $0.99\,I_{\rm lim}$). (d) Concentration and (e) electric potential along the central axis (x axis) as a function of current, $I = 0.3$, 0.6, 0.9, and $0.99\,I_{\rm lim}$. [The incomplete part along the x direction of the curves in (d) and (e) corresponds to the inner disk electrode with radius χ.]

B. Concentration polarization and electric potential

By combining the conformal mapping $f(z)$ in Eq. (17)

$$r = |\xi + \eta i| = |f(z)| = \left|\frac{z-\alpha}{\alpha z - 1}\right|, \tag{20}$$

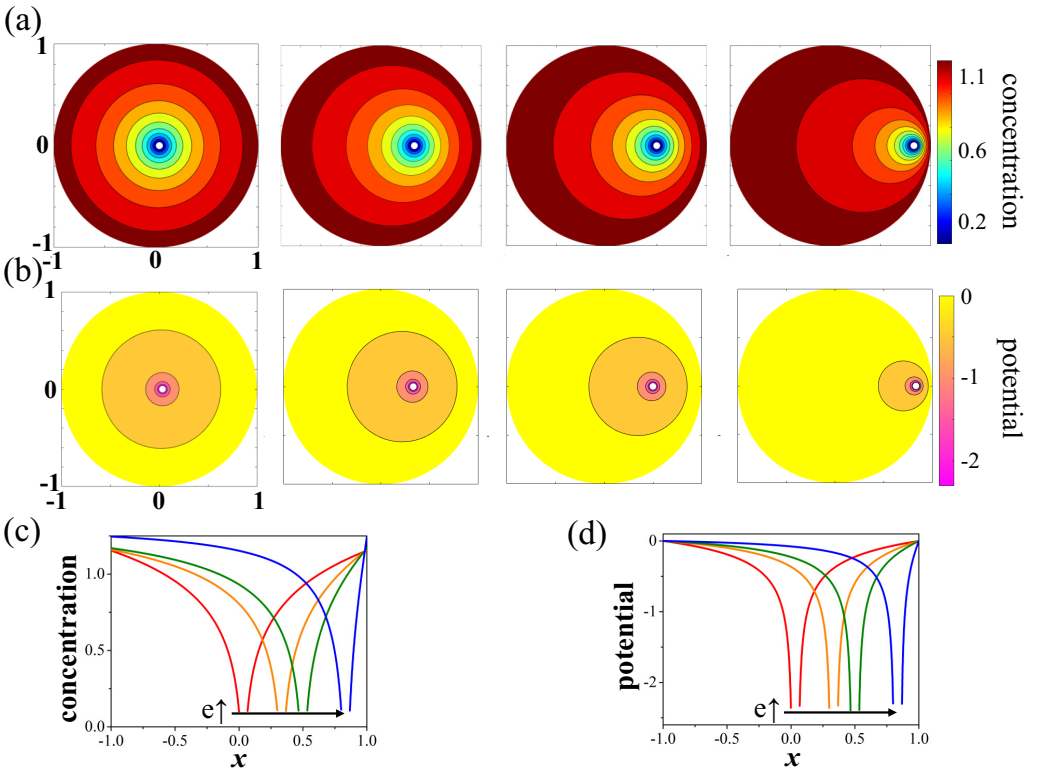

FIG. 3. The effect of eccentricity on concentration polarization and potential distribution in an eccentric annulus ($\chi = 1/30$). (a) Concentration polarization and (b) potential distribution dependent on $e = 1/30, 1/3, 1/2, 5/6$ at $I = 0.9\,I_{\rm lim}$ ($I_{\rm lim}$ is different for each eccentricity, and here the inner electrode is cathode). (c) Concentration and (d) potential along the central x axis [Fig. 2(a)] for $e = 1/30, 1/3, 1/2$, and $5/6$ at $I = 0.9\,I_{\rm lim}$.

with the analytic solutions in Eq. (13), the concentration polarization and electric potential in the eccentric annulus Ω_z are found accordingly,

$$c(z) = 1 - \frac{I}{4\pi}\left(\ln|f(z)| + \frac{1}{2} + \frac{\kappa^2 \ln\kappa}{1-\kappa^2}\right), \tag{21a}$$

$$\varphi(z) = \ln c(z) + \text{const}. \tag{21b}$$

The constrain of the total ion concentration $\mathscr{C}_z$ [Eq. (4)] changes only with a normalization constant in the mapping, but does not affect the mathematical structure of the solution, hence the changing of total concentration $\mathscr{C}_z$ is ignored in the numerical calculation.

For the case of an eccentric annulus with the inner radius $\chi = 1/30$ and the eccentricity $e = 1/2$, by the conformal mapping Eqs. (19a) and (19b), $\alpha = 0.5007$ and $\kappa = 0.0445$. Then by substituting α and κ into Eq. (21), concentration polarization and the electric potential are calculated for various currents (less than the limiting current) in Figs. 2(b) and 2(c). As shown in Fig. 2(d), concentration polarization along the central axis (x axis) increases with the current, and concentration near the cathode approaches to 0 in the limiting current. Also the electric potential at the cathode increases with current [Fig. 2(e)].

For the case of an eccentric annulus with the inner radius $\chi = 1/30$ for a given $0.9I_{\rm lim}$ current, the effect of the eccentricity (e) on concentration polarization and electric potential is shown in the

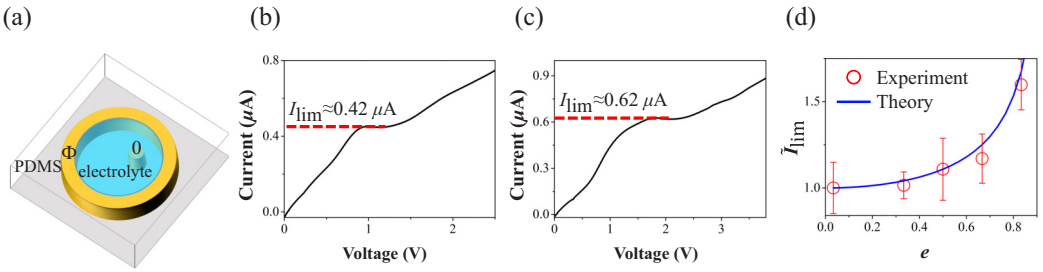

FIG. 4. The effect of eccentricity on the limiting current. (a) Sketch of a PDMS sketch. [(b) and (c)] The I-V curve showing the limit current $I_{\rm lim} \approx 0.42, 0.62\ \mu$A for $e = 1/3, 5/6$, respectively. (d) The measurement of $I_{\rm lim}$ (red circles) agreeing well with the theory of Eq. (14a) (the blue line), and error bars for the standard deviations from five measurements ($\chi = 1/30$).

Figs. 3(a) and 3(b). Also concentration polarization and electric potential along the central axis (x axis) changes with eccentricity [Figs. 3(c) and 3(d)].

C. Limiting current

After mapping to a concentric annulus (an inner radius κ and an outer radius 1) in the ζ plane, the limiting current is directly attained from Eq. (14a) with $\kappa = \kappa(e, \chi)$.

In order to check this theory, we perform experiments to measure the limit current ($\chi = 1/30$). Similarly to the previous experiments [13], the PDMS device with an eccentric circular channel is illustrated in Fig. 4(a), $2R_{\rm inner} = 200\ \mu$m for the inner copper wire, $2R_{\rm outer} = 6$ mm ($\chi = 1/30$) for the outer copper ring, and $H \approx 30\ \mu$m for the channel height. The copper electrodes is combined with the $CuSO_4$ solution by simplifying the system without the unwanted chemical reaction such as electrolysis [12]. The eccentricity is controlled by shifting the inner electrode away from the center of the circle with the distance $d = 0.1$, 1, 1.5, 2, and 2.5 mm, corresponding to $e = 1/30$, $1/3$, $1/2$, $2/3$, and $5/6$, respectively.

The I-V curve is obtained by sweeping the voltage for the 1 mM $CuSO_4$ solution, indicating the limit current is $I_{\rm lim} \approx 0.42, 0.62\ \mu$A for $e = 1/3, 5/6$, respectively [Figs. 4(b) and 4(c)]. The experimental data of the limiting currents (five experiments for each eccentricity e) excellently agree with Eq. (14a) ($\chi = 1/30$) [Fig. 4(d)]. The limiting current $I_{\rm lim}$ increases with e. When the eccentricity ($e \to 1$) approaching to 1 in the physical plane corresponds to the inner radius ($\kappa \to 1$) in the mathematical region, $I_{\rm lim}$ will reach infinity theoretically ($I_{\rm lim} \to \infty$).

D. Electroconvection and deionization shock in OLC

In the experimental I-V curve [Figs. 4(b) and 4(c)] for an eccentric annulus, after the plateau of limiting current, the overlimiting current occurs, i.e., the current continues to increase with the voltage, and electroconvection and the deionization shock might take place. In OLC, no analytic solution in a concentric annulus is available to the best of our knowledge, and the conformal mapping may not be directly applicable to the eccentric annulus. However, since electroconvection in OLC is initially caused by the slip velocity related with the electric field, the electric field and its distribution near the limiting current may still provide theoretical guidance to the electroconvection. Based on Eq. (13b) and (15) together with transformation Eq. (17), the electric field on the cathode is dependent on the angle θ as follows:

$$E_{\rm cathode}(\theta) = \frac{I\frac{|\alpha^2-1|}{|(z-\alpha)(\alpha z-1)|}}{4\pi - I\left(\ln\left|\frac{z-\alpha}{\alpha z-1}\right| + \frac{1}{2} + \frac{\kappa^2 \ln\kappa}{1-\kappa^2}\right)}, \quad z(\theta) = (e + \chi\cos\theta) + i\chi\sin\theta. \tag{22}$$

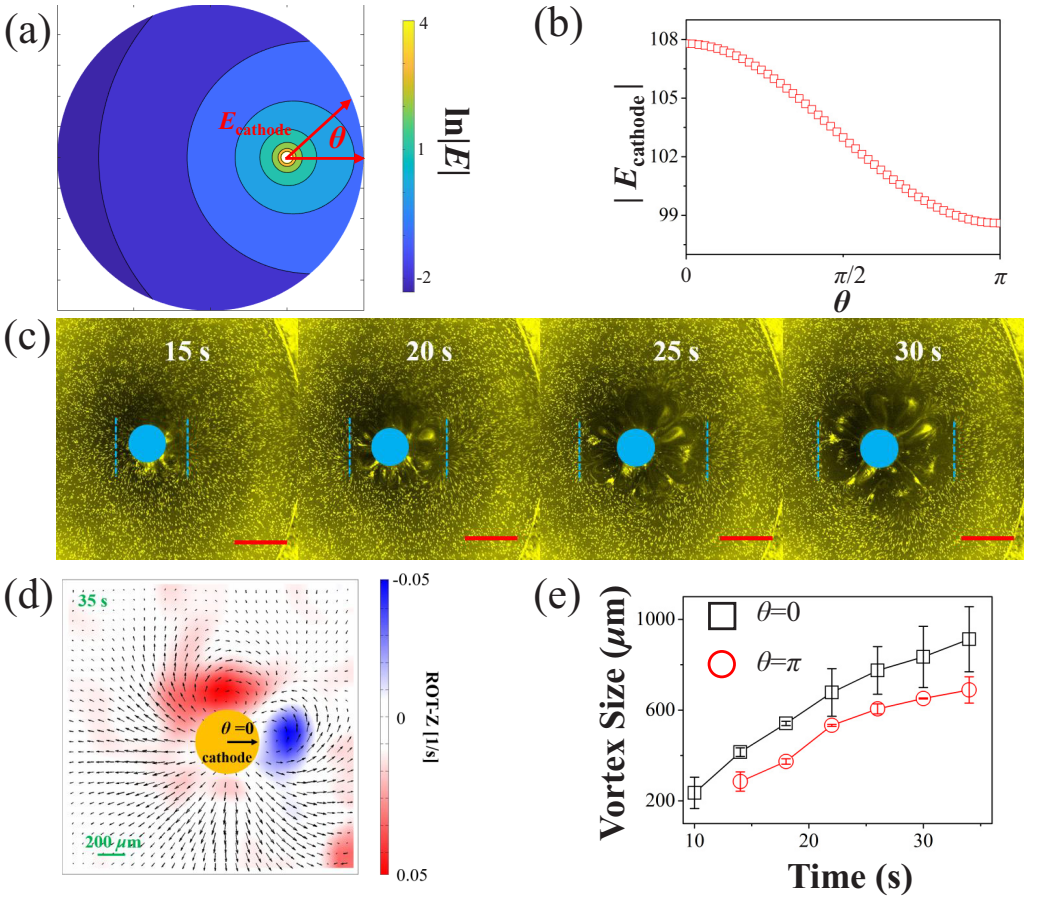

FIG. 5. Electroconvection in OLC. (a) The theoretical electric field distribution with eccentric $e = 1/2$, $\chi = 1/30$, and $I = 0.9\,I_{\rm lim}$. (b) The theoretical electric field on the cathode depends on θ. (c) The snapshots of vortex streamlines in two directions at $t = 15, 20, 25, 30$ s with 4 μA current. The scale bar is 500 μm. (d) PIV images with 2 μA current at $t = 35$ s when the first vortex pair occurs around $\theta = 0$, and the flow speed is about 10 μm/s. (e) The size of vortices [the distance between the blue line and inner electrode in (c)] evolves with time along $\theta = 0,\ \pi$.

For example, at 0.9 $I_{\rm lim}$, the electric field is presented in Figs. 5(a) and 5(b), and the electric field along $\theta = 0$ direction is stronger than that along $\theta = \pi$ direction. Although this anisotropic electric field is calculated under the limit current, one can reasonably argue that a similar anisotropic distribution of electric field still holds in OLC. As the electric field is stronger along $\theta = 0$ direction, the electroconvection is most likely to appear along $\theta = 0$ direction.

To confirm this electroconvection in OLC [13], we carry out experiments in a PDMS device to check the flow and concentration. The geometry parameters are the same as those in Sec. III C, i.e., $2R_{\rm inner} = 200$ μm for the inner copper wire, $2R_{\rm outer} = 6$ mm, and $\chi = 1/30$. The inner electrode is away from the center with $d = 1.5$ mm, then the eccentricity is $e = 1/2$. The solution is 1 mM aqueous $CuSO_4$, and 0.001% 1-μm-diameter fluorescent particles are added into solution to track the flow.

As shown in Fig. 5(c), the evolution of vortices is observed by the fluorescent microscope (Zeiss, Axio Zoom V16) in the OLC at 4 μA (limiting current $I_{\rm lim} \approx 0.42$ μA). At $t = 15$ s, the vortices along $\theta = 0$ direction extend over 400 μm, while the vortices along $\theta = \pi$ direction is

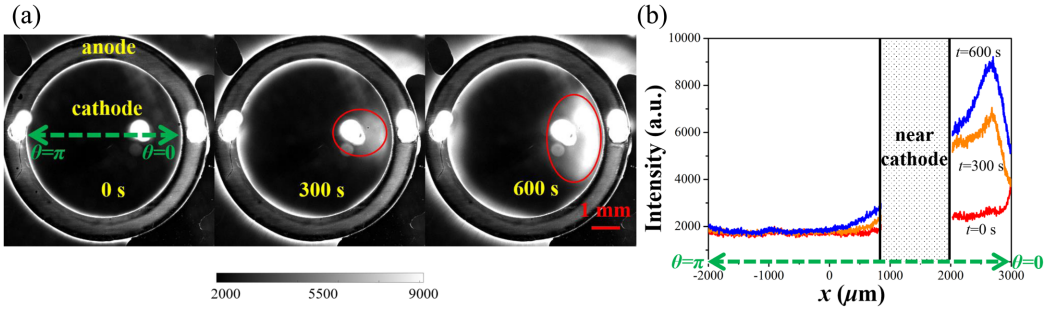

FIG. 6. Deionization shock in OLC. (a) Snapshots of fluorescent signals at 5 μA at $t = 0$, 300, 600 s. The inner electrode is cathode and outer ring is anode. Front of deionization shock is marked by red line, and the brighter region with stronger fluorescent signal is concentration depletion region. (b) The fluorescent intensity along the green line in (a) at $t = 0$, 300, and 600 s, showing that concentration along $\theta = 0$ direction is much more depleted than that along the $\theta = \pi$ direction.

much smaller, only about 200 μm. The vortices continue to grow with time, and the vortex velocity is about 10 μm/s at $t = 35$ s from particle image velocimetry (PIV) [Fig. 5(d)]. Indeed, vortices appeared earlier along $\theta = 0$ direction in most cases of our experiments (six of the eight experiments under a constant current of 2 and 4 μA), as expected from the argument of the stronger electric field along this direction.

Spatiotemporal evolution of concentration is visualized by the fluorescent microscope (Zeiss, Axio Zoom V16), as shown in Fig. 6(a). The concentration of copper ions (Cu^{2+}) was detected by the fluorescent indicator, Phen Green SK dipotassium salt (Invitrogen). The fluorescence intensity of this indicator is quenched by Cu^{2+}, and the increased fluorescence intensity indicates the reduced concentration. The fluorescent indicator is 20 μM, while $CuSO_4$ electrolyte at 10 mM is prepared in a compound solution to enhance the fluorescent signals [13].

The fluorescence intensity along the x direction (or along $\theta = 0, \pi$, a green line) is presented in Fig. 6(b). The fluorescence intensity along $\theta = 0$ direction is much stronger than that along $\theta = \pi$ direction. For example, at $t = 600$ s, the fluorescence intensity along $\theta = 0$ direction is about 9000, while that along $\theta = \pi$ direction is only about 2000. Then the concentration along the $\theta = 0$ direction is much more depleted than that along the $\theta = \pi$ direction. Again this experimental observation is consistent with the argument that the electric field along $\theta = 0$ direction is stronger than that along the $\theta = \pi$ direction to drive the deionization shock [13]. Hence, the electroconvection and deionization shock can be controlled by simply adjusting the position of the inner electrode.

E. EOI of concentration enrichment

When the ratio of inner radius to outer radius is very small in the circular electrode system, electro-osmotic instability can appear near the anode, as the electric field near the inner anode side has a tendency to form singularity [14]. The limiting current is attained from Eq. (14b) by replacing with $\kappa = \kappa(e, \chi)$ in Eq. (19b),

$$I^*_{\rm lim} = 8\pi \frac{(1-\kappa^2)}{1 + 2\kappa^2 \ln \kappa - \kappa^2}, \quad \kappa = \kappa(e, \chi). \tag{23}$$

Then concentration polarization, electric potential, and electric field intensity can be obtained from Eq. (21), as presented in Figs. 7(a)–7(c) ($I = 0.9\, I^*_{\rm lim}$). Similarly to the annular geometry, the concentration is enriched near the inner anode with a maximum value $c_{\rm max}$ [Fig. 7(d)]; a peak of electric field ($E_{\rm anode}$) exists locally near the inner anode [Fig. 7(e)]. As shown in the phase diagram of $c_{\rm max}$ [Fig. 7(f)], $c_{\rm max}$ is enhanced with a smaller χ [14], while decreasing with e. In order to attain

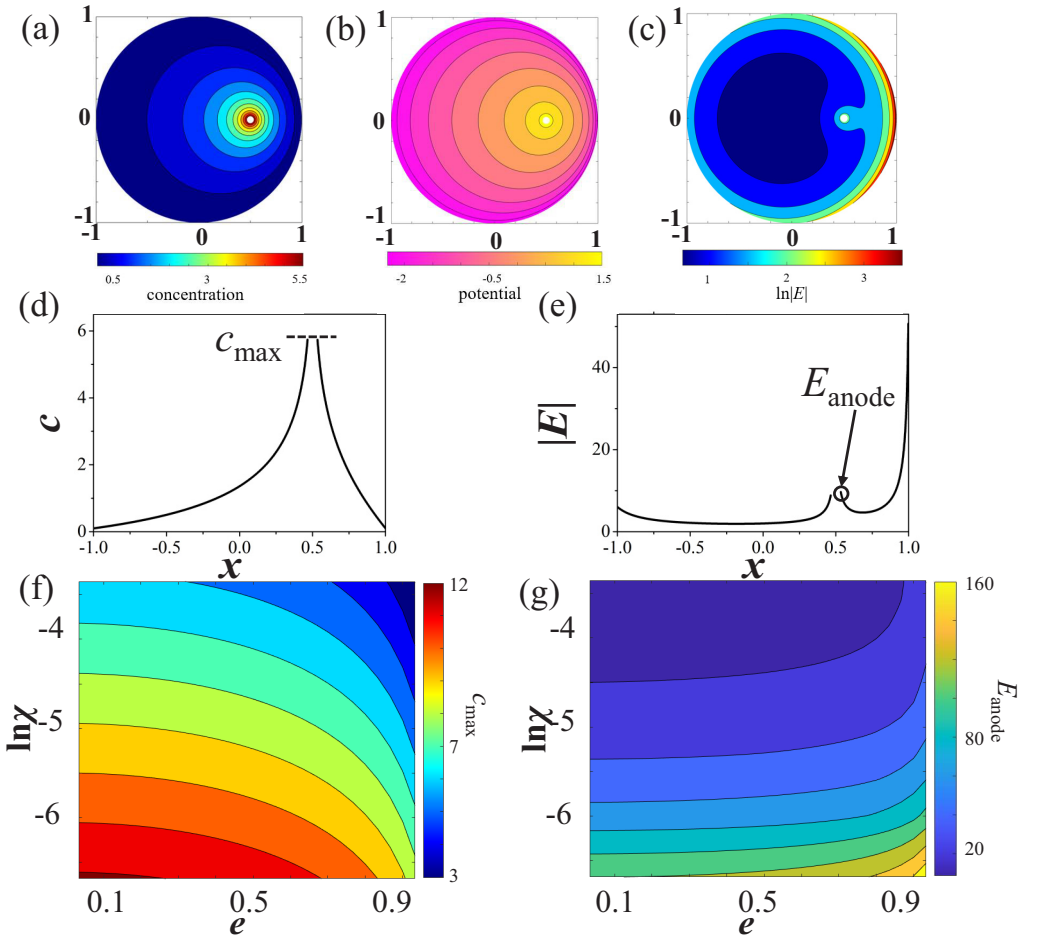

FIG. 7. EOI of concentration enrichment (the inner electrode as the anode). [(a)–(c)] The distribution of concentration, potential, and electric field ($e = 1/2$, $\chi = 1/30$, and $I = 0.9\,I^*_{\rm lim}$). [(d) and (e)] The concentration distribution and the electric field along the central axis [x axis in Fig. 6(a)], showing a maximum value of concentration ($c_{\rm max}$) and a local peak of electric field near the anode ($E_{\rm anode}$). [(f) and (g)] $c_{\rm max}$ and $E_{\rm anode}$ dependent on the eccentricity e and the inner radius χ.

strong concentration enrichment, the anode should be exactly placed at the center of the central circle to circumvent the undesirable displacement.

Furthermore, at the limiting current ($I \to I^*_{\rm lim}$), from Eq. (13a) and (13b), the electric field E_ζ near the anode in a mathematical region Ω_ζ is

$$E_\zeta = -\nabla_\zeta \varphi = -\frac{1}{\kappa \ln \kappa}. \tag{24}$$

Then the maximum electric field intensity on the anode $E_{\rm anode}$ can be obtained by substituting $z = e + \chi$ ($\theta = 0$) in Eq. (15),

$$E_{\rm anode} = -\frac{1}{\ln \kappa} \frac{|\alpha^2 - 1|}{(e + \chi - \alpha)[(e + \chi)\alpha - 1]}. \tag{25}$$

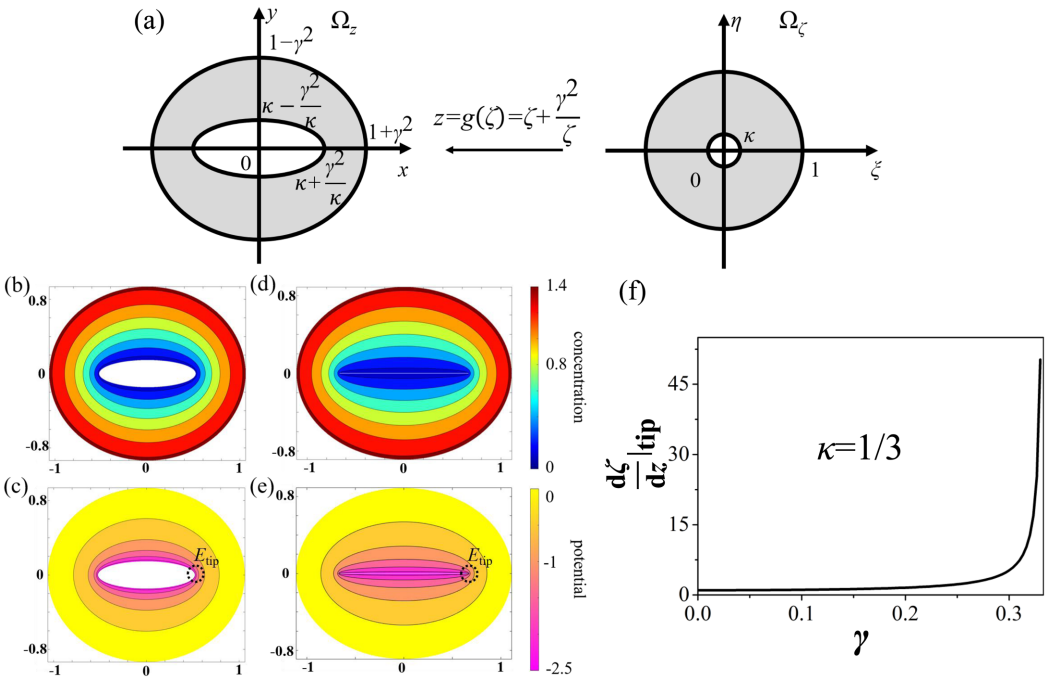

FIG. 8. Conformal mapping calculation of Joukowski transformation ($\kappa = 1/3$). (a) A physical region Ω_z of a concentric ellipse is conformally mapped to a mathematic region Ω_ζ of a concentric annulus. [(b) and (c)] Concentration polarization and electric potential for $\gamma = 1/4$, while [(d) and (e)] for $\gamma = 1/3$ at $I = 0.9I_{\text{lim}}$. (f) $\mathrm{d}\zeta/dz\,|_{\text{tip}}$ changes with γ and diverges as $\gamma \to \kappa$.

As shown in the phase diagram of Fig. 7(g), E_{anode} increases with eccentricity e while decreasing with the inner radius χ. Nevertheless, the eccentricity can be tuned to enhance the electric field in order to achieve EOI of concentration enrichment.

IV. A CONCENTRIC ELLIPSE GEOMETRY

In addition to the eccentric annulus, conformal mapping can be applied to other complicated geometries, such as a concentric ellipse [Fig. 8(a)]. For example, Joukwoski transformation [24]

$$z = g(\zeta) = \zeta + \frac{\gamma^2}{\zeta}, \qquad \zeta = f(z) = g^{-1}(z), \tag{26}$$

maps an annulus Ω_ζ in a mathematical ζ plane $\{\Omega_\zeta \mid \kappa < |\zeta| < 1\}$ to a concentric ellipse Ω_z in a physical z plane ($\gamma < \kappa$)

$$\left\{\Omega_z \middle| \frac{x^2}{(1+\gamma^2)^2} + \frac{y^2}{(1-\gamma^2)^2} < 1,\ \frac{x^2}{\left(\kappa+\frac{\gamma^2}{\kappa}\right)^2} + \frac{y^2}{\left(\kappa-\frac{\gamma^2}{\kappa}\right)^2} > 1\right\}. \tag{27}$$

Here γ is a parameter in the transformation, and κ is the aforementioned inner radius of an annulus in the mathematic plane. When $\gamma = \kappa$, the inner ellipse in Ω_z is degenerated into a stripe (the length is 4κ), and Ω_z is

$$\left\{\Omega_z \middle| \left\{\frac{x^2}{(1+\gamma^2)^2} + \frac{y^2}{(1-\gamma^2)^2} < 1\right\} - \{x \in [-2\kappa, 2\kappa], y = 0\}\right\}. \tag{28}$$

Based on the conformal mapping in Eq. (21), concentration polarization and electric potential in the physical z plane for $\gamma = 1/4, 1/3$, are shown in the Figs. 8(b)–8(e).

Let us study the electric field intensity at the right end of the inner ellipse (stripe) [Figs. 8(c) and 8(e)] in the physical z plane. According to Eq. (15), the electric field in the physical z plane E_z just depends on $|d\zeta/dz|$,

$$\frac{d\zeta}{dz} = \frac{1}{1-\frac{\gamma^2}{\zeta^2}}. \tag{29}$$

Then at the right end or the tip ($\zeta = \kappa$), the corresponding $|d\zeta/dz|$ is obtained as follows:

$$\left.\frac{d\zeta}{dz}\right|_{\text{tip}} = \frac{1}{1-\frac{\gamma^2}{\kappa^2}}. \tag{30}$$

As seen in Fig. 8(f), the $d\zeta/dz\,|_{\text{tip}} \to \infty$ tends to infinite ($\gamma \to \kappa$), and the electric field at the tips of stripe [Fig. 8(e)] forms a singularity. Although the calculation is performed for the inner cathode case, this singularity still holds for the inner anode case.

For EOI of concentration enrichment [14], a general stability criterion based on a bound for the dimensionless local electric field on the anode in the quiescent state is

$$\text{Unstable if}: E \geqslant \frac{k}{\text{Pe}}, \tag{31}$$

where k is a parameter. Therefore, when E_{tip} tends to infinite, this electric field singularity in this concentric ellipse geometry likely drives EOI of concentration enrichment as well.

V. A CORNER GEOMETRY

Besides the aforementioned eccentric annulus and the concentric ellipse, the corner geometry is taken as another example applicable for conformal mapping. As illustrated in Fig. 9(a), the transformation [25]

$$\zeta = \frac{z^n - i}{z^n + i}, \tag{32}$$

maps the infinite Ω_z region in a physical z plane $\{\Omega_z | r > 0, 0 < \theta < \frac{\pi}{n}\}$, to a unit circle Ω_ζ in a mathematical ζ plane $\{\Omega_\zeta | 0 \leqslant r < 1\}$. In particular, the point $\cos(\frac{\pi}{2n}) + i\sin(\frac{\pi}{2n})$ in z plane is mapped to 0 in ζ plane.

Based on the conformal mapping in Eq. (21), for the corner geometry with $n = 1/2, 1, 2, 3$ [Fig. 9(b)], the corresponding concentration polarization and electric potential in the physical z plane are shown in the Figs. 9(c) and 9(d) ($I = 0.9\, I_{\text{lim}}$, $\chi = 1/30$). The circle in the ζ after transformation remains approximately a circle in the z plane by neglecting the shape deformation or distortion of the circle, and then the inner radius of concentric circle κ in the ζ plane is calculated as

$$\kappa = \frac{(\chi+1)^n - 1}{(\chi+1)^n + 1}, \tag{33}$$

where χ is the radius of point electrode in z plane.

The electric field in the corner geometry in a physical z plane is obtained from Eq. (15),

$$E = \frac{I\frac{|2nz^{n-1}|}{|z^{2n}+1|}}{4\pi - I\left(\ln\left|\frac{z^n-i}{z^n+i}\right| + \frac{1}{2} + \frac{\kappa^2 \ln\kappa}{1-\kappa^2}\right)}. \tag{34}$$

For $n = 1/2, 1, 2, 3$, the intensity of the electric field for these four geometries in the physical z plane is shown in Fig. 10(a). Again when $n < 1$ ($n = 1/2$), according to Eq. (34), the electric field appears singularity ($E \to \infty$) as $z \to 0$.

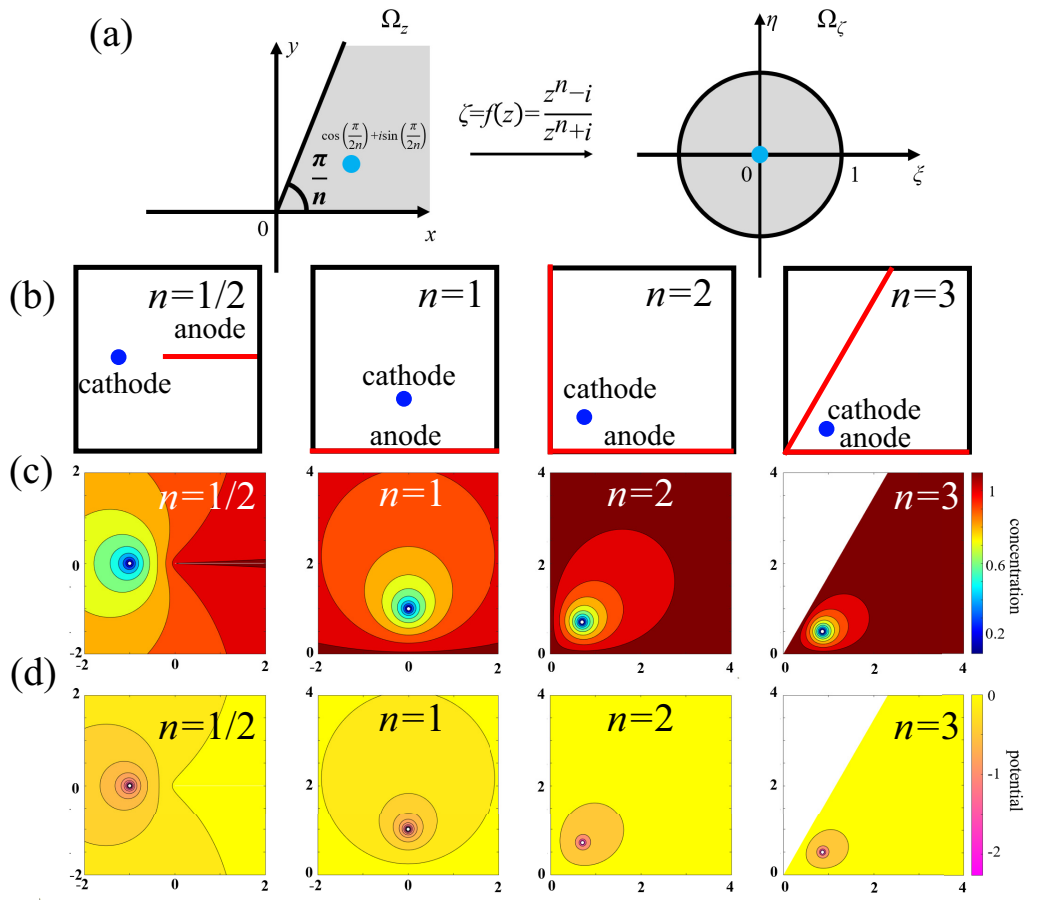

FIG. 9. Conformal mapping calculation in a corner geometry. (a) Physical region Ω_z of a corner geometry is conformally mapped to a mathematica region Ω_ζ. (b) Sketch of the geometry. (c) concentration polarization and (d) electric potential for $n = 1/2$, 1, 2, 3 ($I = 0.9\,I_{\rm lim}$, $\chi = 1/30$).

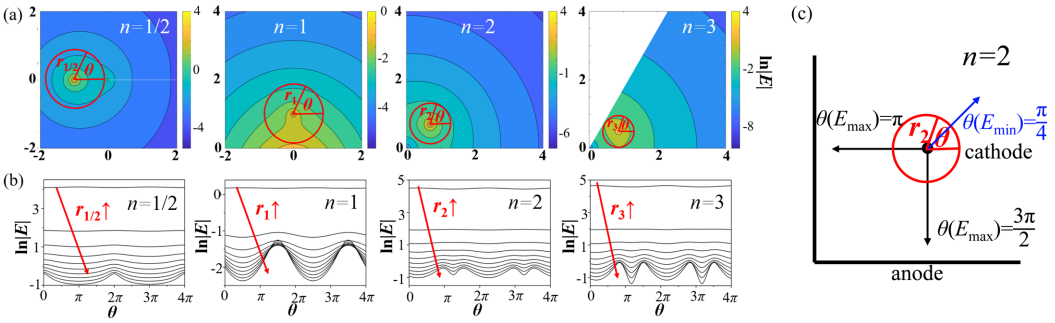

FIG. 10. Distribution of the electric field in a corner geometry. (a) Electric field distribution calculated by conformal mapping at $n = 1/2$, 1, 2, 3 ($I = 0.9\,I_{\rm lim}$, $\chi = 1/30$). (b) The electric field along the red circle in (a), dependent on both θ and r_n. (c) Illustration for $E_{\rm min}$ and $E_{\rm max}$.

The intensity of the electric field becomes more complicated (Fig. 10). For a given red circle centered around the cathode, as shown in Fig. 10(c) for $n = 2$ taken as an example, generally the electric field is determined by both the distance away from the point electrode r_n and its azimuthal direction θ. For $r_n \to \chi$, The intensity of the electric field near the point electrode is isotropic or nearly independent on θ. With the increased distance r_n, the electric field depends on θ and appears anisotropy. For $n = 1/2$, the maximum electric field intensity appears at $\theta = 2\pi$ [$\theta(E_{\max}) = 2\pi$] and the minimum electric field intensity appears at $\theta = \pi$ [$\theta(E_{\min}) = \pi$]; while for $n = 1$, $\theta(E_{\max}) = \frac{3\pi}{2}$ and $\theta(E_{\min}) = \frac{\pi}{2}$. For $n = 2$, $\theta(E_{\max}) = \pi$, $\frac{3\pi}{2}$ and $\theta(E_{\min}) = \frac{\pi}{4}$; while for $n = 3$, $\theta(E_{\max}) = \frac{5\pi}{6}$, $\frac{3\pi}{2}$ and $\theta(E_{\min}) = \frac{7\pi}{6}$. In general, when r_n is large enough [for example in Fig. 10(c)], $E_{\min}$ appears along the direction of the angular bisector, while $E_{\max}$ exits in the direction perpendicular to the corner edge from the point cathode.

VI. DISCUSSIONS AND OUTLOOK

Several aspects on the discussion and outlook are specified as follows.

First, although asymmetries in electrodes and metal particles can amplify or rectify flows for blocking electrodes with little concentration polarization [15,16], here we focus on effects of asymmetry on Faradaic current to electrodes with fast reactions, large concentration gradients and overlimiting current.

Second, the remarkable agreement of the conformal mapping and experimental measurement, such as the effect of the eccentricity on the limiting current in an eccentric annulus (Fig. 4), not only indicates conformal mapping as a powerful mathematical approach is applicable for the ion transport. This agreement also implies that interfacial polarization is indeed negligible to concentration polarization [19].

Third, although having its limitation for a steady or quasisteady state in the electrokinetics, conformal mapping still provides insights into the OLC regime. For example, in an eccentric annulus, the electric field along $\theta = 0$ direction is enhanced by the eccentricity, forming stronger electroconvection and faster propagation of deionization shocks.

Fourth, conformal mapping has the capability to predict the possible intriguing physical phenomena in the complex geometries. For the inner anode case of the eccentric annulus, the phase diagram of E_{anode} dependent on e and χ shows that the increased eccentricity has a more tendency to drive the EOI of concentration enrichment. In a concentric ellipse geometry, when an inner ellipse squashes into a finite stripe, the local electric field at the tips tends to infinite, likely causing the feasibility of EOI of concentration enrichment as well.

Additionally, the conformal mapping and experimental comparison may stimulate more simulation work for electrokinetics in 2D complex geometries, particularly to reveal the electroconvection and the deionization shock.

Last, this theoretical approach of conformal mapping can be applied to more other complicated geometries, which can be mapped to a simple geometry with the available analytical solutions, provided that the geometry transformation is constructed properly in mathematics.

Nevertheless, this mathematical approach certainly has its own certain limitations, mainly arising from only a few of classical mapping functions among the specific shapes, such as the known mapping between a circle to an eccentric circle, as demonstrated here. Once the geometry changes slightly or becomes irregular with symmetry broken, the corresponding mapping function is challenging to be obtained mathematically and can only be approximately fitted with numerical calculation. Also the physical quantity is required to be conformal invariant, in order to be solved by conformal mapping. Additionally, for the case of electrokinetics here, the quantitative calculation is accurately obtained under or near the limiting current; but conformal mapping will be difficult to be performed in OLC, where more complicated phenomena or nonequilibrium physics occur such as extended space charge and electroconvection instability.

In summary, by employing conformal mapping and experimental approach, we explore the electrokinetics (including the concentration polarization, limiting current, electro-osmotic instability

and deionization shocks) in an eccentric annulus, an concentric ellipse and the corner geometry. These results not only generalize the electrokinetic flows and instabilities in 2D complex geometries, enhancing the capability of the particle manipulation and separation in various microfluidic devices through the electrophoresis of polarizable particles [26] or insulator-based dielectrophoresis [27,28], but also offer more opportunities for the deionization shock in 2D complex geometries, in order to realize and optimize the shock electrodialysis for applications such as deionization and removal of the radionuclides from contaminated water [4,5,12].

ACKNOWLEDGMENTS

This work is supported by the National Program in China and startup from Fudan University.

[1] R. F. Probstein, *Physicochemical Hydrodynamics* (Wiley, New York, 2003).
[2] J. Newman and K. E. Thomas-Alyea, *Electrochemical Systems* (Wiley, New York, 2004).
[3] R. B. Schoch, J. Han, and P. Renaud, Transport phenomena in nanofluidics, Rev. Mod. Phys. **80**, 839 (2008).
[4] D. S. Deng, W. Aouad, W. A. Braff, M. E. Suss, M. Z. Bazant, Water purification by shock electrodialysis: Deionization, filtration, separation, and disinfection, Desalination **357**, 77 (2015).
[5] M. A. Alkhadra, K. M. Conforti, T. Gao, H. Tian, and M. Z. Bazant, Continuous separation of radionuclides from contaminated water by shock electrodialysis, Environ. Sci. Technol. **54**, 527 (2020).
[6] T. A. Zangle, A. Mani, and J. G. Santiago, Theory and experiments of concentration polarization and ion focusing at microchannel and nanochannel interfaces, Chem. Soc. Rev. **39**, 1014 (2010).
[7] S. J. Kim, Y. A. Song, and J. Han, Nanofluidic concentration devices for biomolecules utilizing ion concentration polarization: Theory, fabrication, and applications, Chem. Soc. Rev. **39**, 912 (2010).
[8] I. Rubinstein and B. Zaltzman, Electro-osmotically induced convection at a permselective membrane, Phys. Rev. E **62**, 2238 (2000).
[9] B. Zaltzman and I. Rubinstein, Electro-osmotic slip and electroconvective instability, J. Fluid Mech. **579**, 173 (2007).
[10] E. V. Dydek, B. Zaltzman, I. Rubinstein, D. S. Deng, A. Mani, and M. Z. Bazant, Overlimiting Current in a Microchannel, Phys. Rev. Lett. **107**, 118301 (2011).
[11] A. Mani and M. Z. Bazant, Deionization shocks in microstructures, Phys. Rev. E **84**, 061504 (2011).
[12] D. S. Deng, E. V. Dydek, J. Han, S. Schlumpberger, A. Mani, B. Zaltzman and M. Z. Bazant, Overlimiting current and shock electrodialysis in porous media, Langmuir **29**, 16167 (2013).
[13] Z. Gu, B. Xu, P. Huo, S. Rubinstein, M. Z. Bazant, and D. S. Deng, Deionization shock driven by electroconvection in a circular channel, Phys. Rev. Fluids **4**, 113701 (2019).
[14] B. Xu, Z. Gu, W. Liu, P. Huo, Y. Zhou, S. Rubinstein, M. Z. Bazant, B. Zaltzman, I. Rubinstein, and D. S. Deng, Electro-osmotic instability of concentration enrichment in curved geometries for an aqueous electrolyte, Phys. Rev. Fluids **5**, 091701(R) (2020).
[15] M. Z. Bazant and T. M. Squires, Induced-Charge Electrokinetic Phenomena: Theory and Microfluidic Applications, Phys. Rev. Lett. **92**, 066101 (2004).
[16] T. M. Squires and M. Z. Bazant, Breaking symmetries in induced-charge electro-osmosis and electrophoresis, J. Fluid Mech. **560**, 65 (2006).
[17] G. Liu, P. G. Jayathilake, B. Khoo, F. Han, and D. K. Liu, Conformal mapping for the Helmholtz equation: Acoustic wave scattering by a two dimensional inclusion with irregular shape in an ideal fluid, J. Acoust. Soc. Am. **131**, 1055 (2012).
[18] J. A. Miranda, H. Gadelha, and A. T. Dorsey, Coriolis effects on rotating hele-shaw flows: A conformal-mapping approach, Phys. Rev. E **82**, 066306 (2010).
[19] M. Z. Bazant, Conformal mapping of some non-harmonic functions in transport theory, Proc. R. Soc. A **460**, 1433 (2004).

[20] M. Z. Bazant, J. Choi, and B. Davidovitch, Dynamics of Conformal Maps for a Class of Non-Laplacian Growth Phenomena, Phys. Rev. Lett. **91**, 045503 (2003).
[21] M. Bazant and D. Crowdy, Conformal mapping methods for interfacial dynamics, in the *Handbook of Materials Modeling*, edited by S. Yip *et al.*, Volume I: Methods and Models, 4.10 (Springer, Berlin, 2005).
[22] A. Ladd, L. Yu, and P. Szymczak, Dissolution of a cylindrical disk in hele-shaw flow: A conformal-mapping approach, J. Fluid Mech. **903**, A46 (2020).
[23] M. Z. Bazant, Interfacial dynamics in transport-limited dissolution, Phys. Rev. E **73**, 060601(R) (2006).
[24] A. Poozesh and M. Mirzaei, Flow simulation around cambered airfoil by using conformal mapping and intermediate domain in lattice boltzmann method, J. Stat. Phys. **166**, 354 (2017).
[25] A. Bourchtein and L. Bourchtein, Conformal mappings, in *Complex Analysis* (Springer, Berlin, 2021).
[26] S. Oren and I. Frankel, Induced-charge electrophoresis of ideally polarizable particle pairs, Phys. Rev. Fluids **5**, 094201 (2020).
[27] X. C. Xuan, Review of nonlinear electrokinetic flows in insulatorbased dielectrophoresis: From induced charge to joule heating effects, Electrophoresis **43**, 167 (2022).
[28] G. R. Pesch and F. Du, A review of dielectrophoretic separation and classification of non-biological particles, Electrophoresis **42**, 134 (2021).